Defect engineering for improved thermal stability of sulfur hyperdoped silicon

Simon Paulus [a],[*], Sören Schäfer [a], Patrick Mc Kearney [a], Tobias Niemeyer [b], Michael Seibt [b], Stefan Kontermann [b]

[a] Institute for Microtechnologies (IMtech), RheinMain University of Applied Sciences, Am Brückweg 26, 65428, Rüsselsheim, Germany
[b] IV. Physical Institute, University of Göttingen, Friedrich-Hund-Platz 1, 37077, Göttingen, Germany

A B S T R A C T

Sulfur hyperdoped silicon (Si:S) is a promising material for sub-bandgap photovoltaics or infrared photodetectors. However, previous publications show that a temperature step is necessary to improve device performance. This temperature step leads to a decrease in sub-bandgap absorptance, which is a major challenge. We show a post-treatment that increases the thermal stability of Si:S in terms of sub-bandgap absorptance, sheet carrier density and mobility. In addition, we investigate a post-treatment for optical reactivation of Si:S regarding sheet carrier density and mobility and thus gain atomistic insights into the reactivation step.

1. Introduction

Hyperdoping refers to an incorporation of dopants into a host semiconductor material above the thermal solubility limit [1,2]. The resulting pn-junctions formed due to hyperdoping [3] are a promising candidate for applications in intermediate-band photovoltaics or silicon-based infrared photodetectors [4–7]. There are two prominent fabrication methods. First, ion implantation followed by pulsed laser melting PLM (e.g. ns-annealing) [8,9], or second, doping with ultrashort laser pulses [2]. In the latter case, the dopant comes from a gaseous precursor or from a thin layer, deposited on the host material surface. The laser treatment may create a rough surface and crystal defects leading to Urbach tail defects, which further increases the absorptance of the samples [10]. The host material discussed here is silicon and the dopant is sulfur, which forms energy levels deep within the bandgap [11]. Sulfur hyperdoped silicon is also referred to as meta-stable because thermal treatments deactivate the sub-bandgap absorptance [12]. This process is associated with the diffusion of sulfur and the formation of large sulfur clusters or precipitations that are mainly optically inactive [13]. The formation of such precipitations has already been predicted and observed in hyperdoped applications with other dopants (Se, Zn) [14–17]. Besides that, tellurium is a promising dopant, as it has a lower thermal diffusivity and is therefore more stable against thermal processes [9,17]. However, a thermal annealing step seems to be necessary to improve the device performance of e.g. infrared photodetectors [18–20].

A lot of research effort has gone into understanding the deactivation mechanism of sub-bandgap absorptance [12,21,22]. Previous studies found that the optical deactivation is correlated to the sulfur diffusion length in bulk silicon. Simmons et al. propose three chemical states that occur during annealing [12]. They assigned the initial, optically active state to isolated substitutional sulfur impurities (in the rest of the manuscript we refer to these as sulfur monomers). After low temperature treatments, i.e. short sulfur diffusion lengths, they report a reduction in sub-bandgap absorptance that comes along with a slight increase in sheet carrier density. Both findings can be explained by the formation of sulfur-dimers, which lead to shallower defect levels in the silicon bandgap, according to Janzén et al. [23]. This first transition can be described as follows.

$$\text{sulfur-monomers} \rightarrow \text{sulfur-dimers} \tag{1}$$

If higher sulfur diffusion lengths are attained, a third sulfur state is formed as a prominent one. It is characterized by a low sheet carrier density and low sub-bandgap absorptance, due to the formation of sulfur clusters. We can describe this process as follows.

$$\text{sulfur-dimers} \rightarrow \text{sulfur-clusters} \tag{2}$$

The predominant reaction also depends on the initial distribution of sulfur states. Limaye et al. investigated the different sulfur impurities of laser hyperdoped silicon using core-level x-ray photoelectron

spectroscopy [24]. They found sulfur monomers i.e. S^0 and S^{2-} respectively, but also sulfur dimers, especially S_2^-. In addition, they observed other sulfur species such as SO_3^{2-}/SO_4^{2-} and sulfur clusters S_n^{2-}, where n > 2 refers to larger sulfur clusters. Limaye et al. found the concentration of sulfur-monomers, sulfur-dimers and clusters to be 32.4 %, 22.1 % and 24.5 % respectively in the *as*-hyperdoped state [24]. However, due to a temperature treatment at 700 °C Limaye et al. observe an increasing proportion of sulfur clusters whereas the concentration of sulfur monomers vanishes.

Furthermore, it was shown that sub-bandgap absorptance can be reactivated through adapted annealing methods. Newman et al. observed that it can be slightly increased by a temperature step at 1510 K followed by quenching with a cooling rate of 250 K/s [25]. They found that temperatures above 1350 K are necessary to enable this reactivation and assume that below this temperature the sulfur states that form an intermediate band are unstable and decrease, whereas at temperatures above 1350 K these sulfur point defect i.e. monomer states can remain stable [26]. Franta et al. showed that an even larger fraction of sub-bandgap absorptance can be reactivated by processing the hyperdoped silicon with nanosecond laser pulses [27,28]. This process is referred to as nanosecond-annealing (ns-annealing) and induces temperatures above 1350 K while enabling high cooling rates and thus more solute trapping takes place, i.e. more sulfur can be trapped in optically active sulfur monomer states, compared to Newman et al. Mc Kearney et al. presented another pulsed laser-based annealing method for reactivation, referred to as ultrafast laser heating (ULH) [29,30]. This method is based on heat accumulation of ultrashort laser pulses at high repetition rates. As with ns-annealing, the temperature of the surface can be adjusted by varying the laser fluence. However, with ULH the time scale is in the range of a few 10 μs for the heating and cooling time of the sample, and not in the nanosecond scale compared to ns-annealing. The reported results achieved by ULH and ns-annealing are comparable in terms of sub-bandgap absorptance.

As discussed, much effort has gone into understanding the deactivation mechanism of meta-stable hyperdoped silicon, but the mechanism of reactivation of sub-bandgap absorptance remains largely unknown. In this work, we optically reactivate sulfur hyperdoped silicon by ULH and characterize it with respect to the resulting sub-bandgap absorptance, charge carrier density and mobility. Our results provide a better understanding of optical reactivation and give an insight into the transformation processes of the atomistic states of sulfur that take place during the applied post hyperdoping processes. Furthermore, we show that the temperature stability of Si:S can be increased with respect to sub-bandgap absorptance, sheet carrier density and carrier mobility if an ULH step is performed preliminary to minute-long thermal annealing. Thermal stability is a crucial challenge in fabrication of optoelectronic devices. Until now, it is necessary to ensure that the temperature budget after fabrication is kept low to prevent dopant diffusion [31]. A process to increase thermal stability is therefore of great interest for both research and application [32,33]. Finally, we develop a model to explain our experimental findings.

2. Experimental

We produce sulfur-hyperdoped silicon by scanning ultrashort laser pulses (Amplitude Tangor 100) over a silicon surface in a sulfur-hexafluoride containing atmosphere. This is followed by one or two annealing steps, whereby two different thermal processes are used, which exhibit different time scales. The first step is a minute-long thermal annealing process on a hotplate at different temperatures for 30 min, whereby the temperature steps are carried out consecutively. After this treatment, the samples are cooled in ambient air, which corresponds to a cooling rate of approx. 50 K/s [25]. The second annealing process is ULH, which takes place on a timescale of several tens of μs. We use laser fluences of 10 mJ/cm², 15 mJ/cm² and 20 mJ/cm² to achieve surface temperatures of up to 2000 K, 3000 K and 4000 K respectively

Table 1
Experiment plan including applied process parameters. All samples are sulfur laser-hyperdoped and cleaned, followed by up to two annealing steps.

fabrication	first anneal	second anneal	name

laser-parameters:
• pulse duration: 10 ps
• wavelength: 1030 nm
• fluence: 1.4 J/cm²
• repetition rate: 200 kHz
• spot diameter: 70 μm
• pulse distance:
  $\Delta x = \Delta y = 2.8$ μm
  $\triangleq$ 500 pulses per spot
• v_{scan} = 555 mm/s
 	
gas-atmosphere:
• gas: sulfurhexafluoride SF_6
• pressure: 675 mbar
• flow rate: 500 sccm
 	
cleaning:
• acetone + IPA + DIW drinse
• brushed in DIW + surfactant
• acetone + IPA + DIW drinse
	-	**-**	**as lasered**

	300 °C … 550 °C, 30 min	**-**	300C … 500C
	TH 600 °C, 30 min	**-**	**TH**
		ULH1	TH+ULH1
		ULH2	**TH+ULH2**
		ULH3	TH+ULH3
	ULH 1 **laser-parameters:** • 10 ps, 41 MHz, 3 m/s, Δx=0.07 μm, Δy=2.5 μm • fluence: 10 mJ/cm²	**-**	ULH1
		300 °C … 500 °C 30 min	ULH1+300C … ULH1+550C
		600 °C, 30 min	ULH1+TH
	ULH 2 • ULH1 but fluence: 15 mJ/cm²	**-**	**ULH2**
		300 °C … 550 °C 30 min	ULH2+300C … ULH2+550C
		600 °C, 30 min	**ULH2+TH**
	ULH 3 • ULH1 but fluence: 20 mJ/cm²	**-**	ULH3
		300 °C … 550 °C 30 min	ULH3+300C … ULH3+550C
		600 °C, 30 min	ULH3+TH

[29]. The cooling rates of this annealing method are in the range of several 1000 K/s. An overview of the applied process parameters is shown as an experimental plan in Table 1.

For the electrical characterization experiments, a high-resistance substrate (FZ, 2000–8000 Ωcm, p-type, double side polished, 280 μm) is used to ensure the formation of a pn-junction between the laser-hyperdoped layer and the substrate. The samples are cleaned with acetone, isopropanol (IPA) and DIW before they get brushed in deionized water (DIW) + surfactant solution to remove dust that originates from the laser process. Afterwards they are cleaned again with acetone IPA and DIW. After cleaning the samples are subjected to the various annealing steps according to Table 1. For metallization an HF dip for 5 min in 1% HF is performed and Cr/Au (30 nm/130 nm) contacts are deposited by magnetron sputtering. The samples are then cut into 10×10 mm^2 squares with the metal contacts in the corners. For characterization, the samples are contacted with gold bonding wires.

The van der Pauw measurements are performed in the dark and at room temperature. We use a magnetic field with 0.45 T to perform the Hall measurements. The used current varies according to the sample between 100 μA and 500 μA.

The other characterizations and measurements are carried out on hyperdoped samples which have been processed on a different substrate (CZ, 1–10 Ωcm, p-type, 380 μm, double side polished). They were prepared according to Table 1, however, in a round geometry (r = 15 mm). We investigate the surface morphology with a scanning electron microscope (JEOL JSM-6380 L V) with the surface tilted by 30°. We characterize the optical properties of the samples with a spectrophotometer (PerkinElmer Lambda 750) with a center mount to place the samples directly inside an integrating sphere [34]. The sulfur doping concentration profile is measured with a secondary ion mass spectrometer (SIMS) (Cameca ims 4f-E6) using 14.5 keV Cs$^+$ ions. The crater dimension is 50×50 μm^2, the depth information and sulfur concentration are calibrated with a reference Si:S standard. To determine the crystallinity, we utilise a Raman spectrometer (DXR3 by Thermo Fischer Scientific) equipped with a laser operating at 785 nm and 30 mW.

3. Results

The laser-hyperdoping step creates a rough needle-shaped silicon surface, a SEM micrograph of an *as*-lasered samples is shown in Fig. 1 a). The sulfur doping profile of this sample, measured with SIMS is shown in Fig. 1 b). It corresponds to former SIMS measurements on fs-laser hyperdoped silicon [35]. In addition, the doping profiles of Simmons et al. and Wang et al. are shown as well. The hyperdoped layer thicknesses of Simmons and Wang et al. are in the range of a few hundred nanometers and have a higher local doping concentration compared to the *as*-lasered samples. However, the *as*-lasered samples show a doping profile that extends up to 3 μm deep into the silicon.

Fig. 1 c) shows the average sub-bandgap absorptance of the samples

printed in bold in Table 1, where Ā refers to the absorptance value averaged from 1500 to 2300 nm. After hyperdoping the sub-bandgap absorptance is above 90 %. A minute long thermal post-treatment (TH) leads to a strong decrease in sub-bandgap absorptance to (15.7 ± 3.3) %. However, if the thermal treatment is applied after the ULH2 step (i.e. ULH2+th) the sub-bandgap absorptance only decreases to (32.3 ± 2.5) %.

If the last annealing step that is applied is a ULH step, the sub-bandgap absorptance is significantly higher. The ULH2 results in a comparable infrared absorption as in the *as*-lasered state. Additionally, if the samples were optically deactivated by a thermal step, a subsequent ULH2 step reactivates the sub-bandgap absorptance to (68.8 ± 3.3) %. The sequence in which the annealing steps are applied therefore has an influence on the resulting material properties of the hyperdoped layer.

To combine temperature values and annealing duration in one parameter, the sulfur diffusion length was calculated according to equation (3).

$$l_{diff} = \sqrt{D_0 \times t \times e^{-\frac{E_A}{k_B T}}} \tag{3}$$

Where $D_0 = 0.92$ cm^2/s and $E_A = 2.2$ eV are temperature independent parameters for the diffusion of sulfur in bulk silicon [36,37]. Further, t is the annealing duration, k_B is Boltzmann's constant and T is the annealing temperature. Fig. 2 a) shows the deactivation of sub-bandgap absorptance as a function of the sulfur diffusion length. However, our data indicates that samples annealed with an ULH step preliminary to the thermal annealing show a less pronounced decrease in sub-bandgap absorptance compared to the *as*-lasered samples. All ULH samples result in a higher sub-bandgap absorptance after a 600 °C temperature step (corresponding to a diffusion length of 182 nm in Fig. 2 a).

Fig. 2 b) shows the sheet carrier density as a function of sulfur diffusion length. The *as*-lasered samples and the ULH1 samples show a high n-type sheet carrier density of 1.47×10^{15} cm^{-2} and 1.09×10^{15} cm^{-2} respectively. Due to a subsequent thermal annealing and thus diffusion of silicon the sheet carrier density decreases to 2.41×10^{14} cm^{-2} and 2.65×10^{14} cm^{-2} respectively. In addition, reported values form literature are shown.

For the ULH2 and ULH3 samples the sheet carrier density is significantly lower in the initial state (3.67×10^{13} cm^{-2} and 4.01×10^{13} cm^{-2}) and increases slightly with increasing diffusion length. We measure maximum values of 5.60×10^{13} cm^{-2} and 5.46×10^{13} cm^{-2}, after a diffusion length of 39 nm and 114 nm respectively. However, the last minute-long thermal annealing step, i.e. TH results in a sheet carrier density of 4.44×10^{13} cm^{-2} and 4.32×10^{13} cm^{-2} respectively, the charge carrier density is still higher than the initial value for the ULH2 and ULH3 samples.

The TH samples are optically reactivated by subjecting them to a ULH2 or ULH3 step. This reduces the sheet carrier density from the initial value $n_{s, TH} = 2.41 \times 10^{14}$ cm^{-2} to 4.31×10^{13} cm^{-2} and
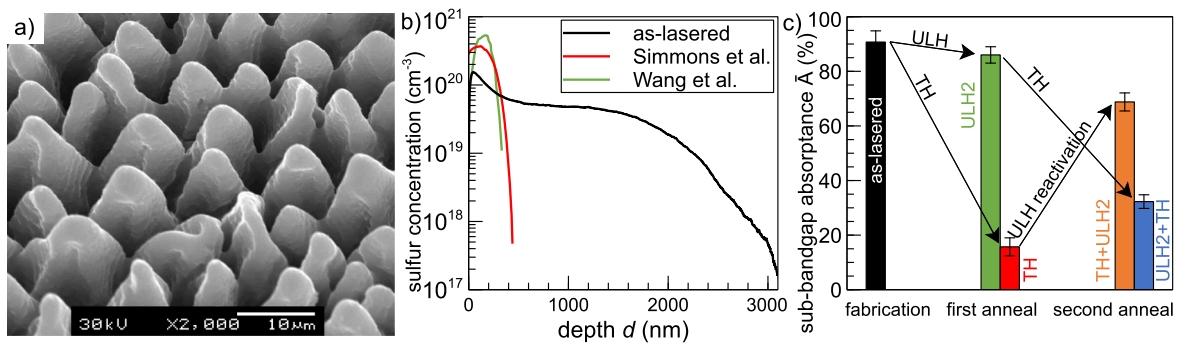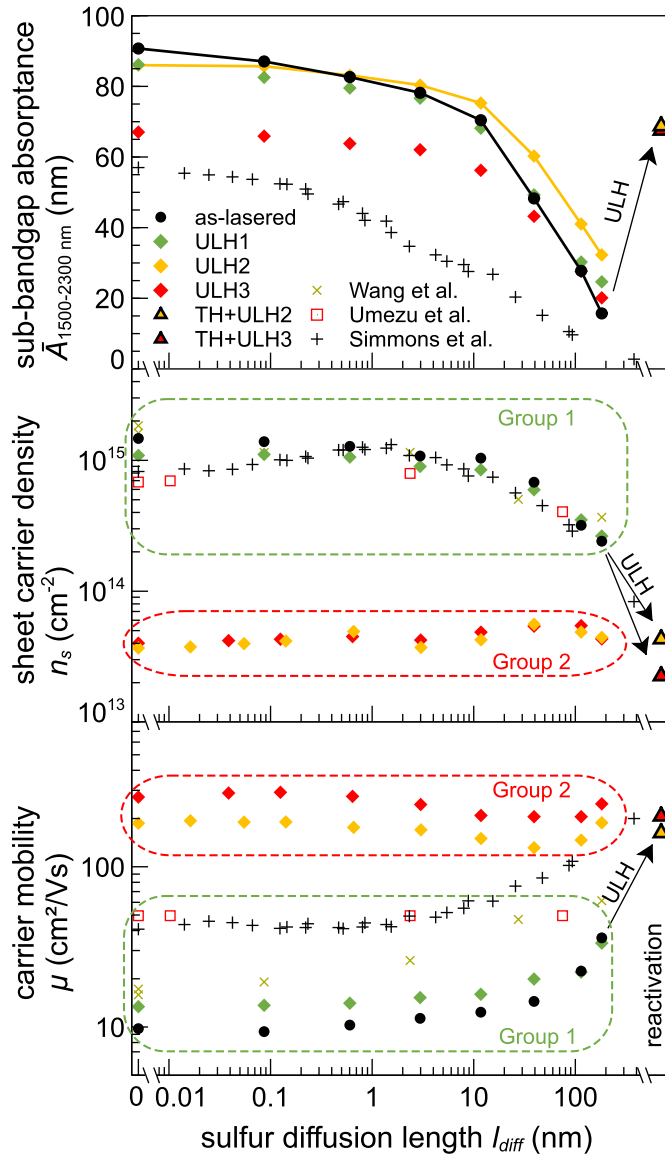

Fig. 1. a) SEM micrograph of an *as*-lasered sample tilted by 30°; b) doping profile measured with SIMS of an *as*-lasered sample, and from literature reported doping profiles, where ion implantation was used for hyperdoping [12,21]; c) sub-bandgap absorptance averaged from 1500 to 2300 nm for the samples printed in bold in Table 1.

Fig. 2. a) sub-bandgap absorptance averaged from 1500 nm to 2300 nm as a function of sulfur diffusion length. Literature values of Simmons et al. are plotted as well [12]. After the TH step i.e. 182 nm diffusion length, all ULH samples show a higher sub-bandgap absorptance compared to the *as*-lasered sample. The sub-bandgap absorptance of the TH samples can be reactivated with an ULH step; b) sheet carrier density as a function of the diffusion length. Two groups are identified. In Group 1, the sheet carrier density decreases by almost an order of magnitude due to sulfur diffusion, whereas Group 2 shows no significant change. Reported values from the literature are plotted as well. [11,12,21]; c) mobility as a function of the diffusion length, whereby the same groups are identified. Group 1 shows an increase in mobility with increasing diffusion length, whereas Group 2 is less sensitive. Again literature values are plotted [11,12,21].

2.25×10^{13} cm^{-2} respectively.

Fig. 2 c) shows the carrier mobility as a function of sulfur diffusion length. The *as*-lasered samples and the ULH1 samples show a similar trend starting at a mobility of 9.8 cm^2/Vs and 13.4 cm^2/Vs, and then increasing to a value of 36.0 cm^2/Vs and 33.0 cm^2/Vs, respectively. Again, values from the literature are plotted as well. The optical reactivation step of the samples TH + ULH2 and TH + ULH3 leads to 163 cm^2/Vs and 207 cm^2/Vs respectively.

The samples ULH2 and ULH3 exhibit carrier mobilities of 187 and 272 cm^2/Vs respectively after applying the ULH treatment. After the

minute-long thermal annealing, the mobility remains almost unchanged at 188 cm^2/Vs and 247 cm^2/Vs respectively.

4. Discussion

4.1. Doping-profile

From Fig. 1 b) we can assume that the doping profiles differ according to the used fabrication method, with laser hyperdoping reaching deeper into the material, whereas higher local sulfur concentrations can be achieved by ion implantation. However, Simmons et al. and Wang et al. used ion implantation followed by a ns-annealing step to hyperdope the silicon, and the sulfur concentration depth profile from Wang et al. is based on simulations and is not measured with SIMS [12,21]. However, it must be considered that the rough, needle-structure of our samples (Fig. 1 a) makes it difficult to interpret the SIMS profiles, as the surface structure results in non-linear removal rates and thus to inaccuracies in the depth information.

Simmons et al. mention that their interpretation (which we presented in section 1) can alternatively be explained by the local dopant concentrations. Although the measured doping profiles here show differences to Simmons et al. the observed sheet carrier density as a function of sulfur diffusion length (Fig. 2 b) is consistent. According to this result the cited primary discussion of Simmons et al. is supported. The model developed in subsection 4.4 is based on this interpretation.

4.2. Sub-bandgap absorptance

In accordance with Simmons et al. minute long thermal annealing decreases the sub-bandgap absorptance of Si:S (see Fig. 2 a). Simmons et al. examined samples that have a flat surface morphology and thus, the total absorption is lower compared to our samples. However, the sub-bandgap absorptance of ULH samples proves to be more stable for thermal annealing, compared to the *as*-lasered samples. This observation represents a great benefit for sulfur hyperdoped applications, as the low thermal budget of Si:S was one of the major reasons to investigate other elements for hyperdoping [31,32]. In addition, if optically deactivated samples (i.e. TH) undergo a ULH step, they are optically reactivated (see Fig. 1 c). The reactivation originates from the high temperatures and cooling rates achieved with ULH and indicate that the sulfur impurities undergo a state modification so that more sulfur is then present as an optically active sulfur monomer [25,27,29].

Wen et al. reported a temperature-stable sulfur state with respect to sub-bandgap absorptance for ns-fabricated Si:S. However, they use reflection and transmission measurements to calculate the absorptance, which leads to an offset, since light is scattered laterally by the rough surface and is not captured from the integration sphere [34]. When using the same method to determine the absorptance as Wen et al. ($A = 1 - R - T$), we observe an error of up to 34 %, shown in Fig. S2. The absorptance values are therefore difficult to compare.

4.3. Sheet carrier density and mobility

Based on the results in Fig. 2, we distinguish between two different groups of samples with different behavior to thermal heating, i.e. to sulfur diffusion. Group 1 consists of the *as*-lasered and the ULH1 samples. The ULH2 and ULH3 samples, referring to as Group 2, show a different trend if subjected to thermal annealing, especially regarding the electrical characterization.

The findings of Group 1 are in good agreement with values from the literature, also shown in Fig. 2 b). In contrast, the stability of the sheet carrier density and mobility by thermal treatments of Group 2 is new. In the next subsection, an approach to explaining these observations is made.

The increase in mobility with increasing sulfur diffusion length observed for Group 1 in Fig. 2 c) is also reported in the literature, but with

an offset towards higher carrier mobilities. We suspect that this offset is due to the literature samples being fabricated with ion implantation followed by a ns-annealing step. As a result, the crystallinity of the hyperdoped layer should be higher and fewer amorphous silicon phases are present than in the laser doping fabrication we use, thus leading to less scattering at crystal defects i.e. higher carrier mobilities [38].

Fig. S1 gives insights into factors that influence the carrier mobility. Literature suggests that carrier density is the limiting factor for mobility in Si:S [21,26]. On the other hand, scattering from lattice defects as well as from free carriers is typically associated with a low carrier mobility [39,40]. However, our results show that both a low fraction of amorphous silicon and a low charge carrier density are crucial to achieve high mobilities.

4.4. Model for defect engineering of Si:S

In this subsection, we develop a model which explains the experimental findings. According to Simmons et al. we assume that sulfur can exist in three different states: i) as sulfur monomers, which generate energy states deep in the bandgap of silicon and thus enable subbandgap absorption, but do not provide free carriers; ii) sulfur dimers, which introduce energy states closer to the band edge of silicon and thus do not enable sub-bandgap absorption, but contribute charge carriers to the conduction band at room temperature; and iii) sulfur clusters, which introduce energy states even closer to the band edge and thus do not enable sub-bandgap absorption. In addition, because many sulfur atoms are involved in one cluster, the net charge carriers provided by one sulfur atom is lower, compared to sulfur dimers.

Our experimental findings can then be explained if one assumes that different fabrication processes and annealing methods lead to different concentrations of these sulfur defect states. Group 1 is characterized by its initially high sub-bandgap absorptance, high sheet carrier density and low charge carrier mobility. Therefore, to consider these observations we assume that in Group 1 the sulfur is present both as monomer, causing high sub-bandgap absorptance, and dimer, being responsible for the high sheet carrier density. This assumption is supported by the findings of Limaye et al. which we discussed in the first section, whereby they additionally report a sulfur-cluster concentration of 24.5 % [24].

We illustrate this initial state in Fig. 3 a). There, the respective defect state energy is schematically represented by the distance to the edge of the conduction band. According to Janzén et al. [23], sulfur-clusters form shallow defects, followed by dimers and final monomers, which form the deepest defects near the band gap middle, up to 618 meV below the CB [23]. Fig. 3 b) lists quantitative measured values in a tabular form for the samples printed in bold from Table 1.

Group 2 exhibits a charge carrier density more than one order of magnitude lower, and a mobility more than one order of magnitude higher, compared to Group 1. This behavior of Group 2 indicates different concentrations of the sulfur states. The low charge carrier density suggests that the concentration of sulfur dimers and sulfur clusters is small. The high sub-bandgap absorptance indicates that a high concentration of sulfur monomers is present, forming an intermediate band [11,12,41]. This is sketched schematically in Fig. 3 a).

This model explains the different thermal behavior of the samples. Group 1 samples lose their sub-bandgap absorptance due to thermal annealing because the concentration of sulfur monomers decreases, and sulfur dimers and sulfur clusters are formed due to transition (1) and (2). For Group 1, the ratio of transition (2) is larger than transition (1), which results in a net decrease of charge carrier density because more sulfur dimers continue to react through transition (2) than new ones are formed through transition (1). This is because a large number of sulfur dimers are initially present in Group 1, which can undergo transition (2) directly. On the other hand, according to our model, samples of Group 2 initially have a higher proportion of sulfur monomers, compared to dimers. Therefore, transition (1) is preferred over transition (2) compared to Group 1 and thus no decrease in carrier density is observed. This also explains the increase in charge carrier density initially by about 53 %. However, after long diffusion lengths, samples of Group 2 show a higher thermal stability regarding the electrical and optical properties compared to Group 1. This is due to the higher initial concentration of substitutional sulfur monomers, which are responsible for the formation of an intermediate band and thus sub-bandgap absorptance.

By applying an ULH step to Group 1 samples, which have been thermally annealed (i.e. Group 1 + TH), the sheet carrier density decreases significantly to 4.4×10^{13} cm^{-2}. Thus, suggesting that sulfur dimers and sulfur-clusters are converted to sulfur-monomers, which contribute less carrier to the conduction band as they are located so deep within the silicon band gap. Therefore, sulfur-monomers are the
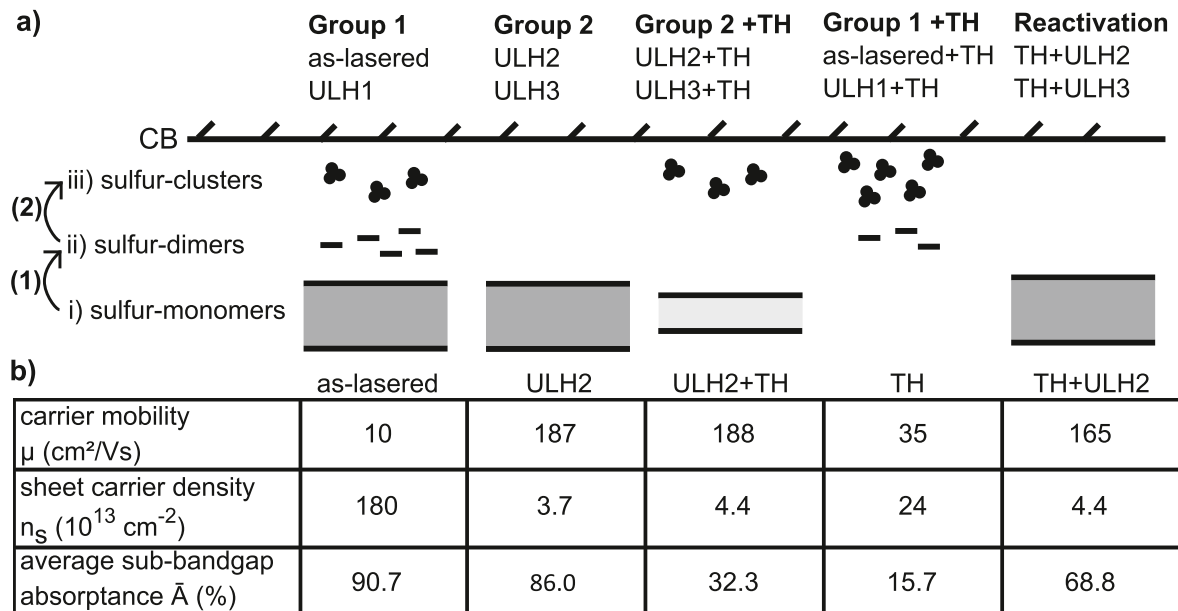

b)	as-lasered	ULH2	ULH2+TH	TH	TH+ULH2
carrier mobility μ (cm²/Vs)	10	187	188	35	165
sheet carrier density n$_S$ (10^{13} cm^{-2})	180	3.7	4.4	24	4.4
average sub-bandgap absorptance Ā (%)	90.7	86.0	32.3	15.7	68.8

Fig. 3. a) shows the groups identified from Fig. 2 with assigned sulfur defect states. The states are arranged according to their energy distance to the silicon conduction band, according to Janzén et al. [23]. The sulfur states change due to thermal annealing according to transition (1) and (2) which refer to Simmons et al. and are explained in detail in the introduction section [12]; b) shows measured values for representative samples printed in bold in Table 1.

predominant atomistic sulfur configuration. This leads to an increase in sub-bandgap absorptance, hence optically reactivating the material.

5. Conclusion

Our observations support the assumption that minute-long thermal annealing leads to a reduction in the concentration of sulfur monomers and the formation of sulfur clusters. Furthermore, the concentration of different sulfur states depends on the fabrication or annealing method used. Laser hyperdoping with picosecond laser pulses shows good agreement with ion-implanted samples, with regards to the electrical and optical behavior due to thermal treatment. However, heating the surface in the microsecond time scale by ULH with cooling rates in the range of 1000 K/s leads to an increase of sulfur monomers in the hyperdoped layer. In terms of its electrical properties, this state is much more stable against thermal annealing; the charge carrier density and mobility are not significantly changed due to a thermal treatment at 600 °C for 30 min. Also, the optical properties are less affected by thermal processing, indicating that the thermal budget is higher for these samples. All ULH samples show higher sub-bandgap absorptance than the *as*-lasered samples after thermal treatment. Furthermore, our results suggest that ULH can be used to optically reactivate Si:S by changing the atomistic sulfur configuration to predominantly sulfur-monomers.

CRediT authorship contribution statement

Simon Paulus: Writing – original draft, Investigation, Conceptualization, Methodology, Validation, Formal analysis, Visualization, Data curation. **Sören Schäfer:** Writing – review & editing, Supervision, Project administration, Methodology, Conceptualization. **Patrick Mc Kearney:** Writing – review & editing, Supervision, Resources, Methodology, Conceptualization. **Tobias Niemeyer:** Writing – review & editing, Supervision, Project administration, Methodology, Conceptualization. **Michael Seibt:** Writing – review & editing, Supervision, Project administration, Methodology, Funding acquisition, Conceptualization. **Stefan Kontermann:** Writing – review & editing, Supervision, Project administration, Funding acquisition, Conceptualization.

Declaration of competing interest

The authors declare that they have no known competing financial interests or personal relationships that could have appeared to influence the work reported in this paper.

Data availability

Data will be made available on request.

Acknowledgement

Appendix A. Supplementary data

Supplementary data to this article can be found online at https://doi.org/10.1016/j.mssp.2024.108297.

References

[1] Z. Tong, M. Bu, Y. Zhang, D. Yang, X. Pi, Hyperdoped silicon: processing, properties, and devices, J. Semiconduct. 43 (2022) 93101, https://doi.org/10.1088/1674-4926/43/9/093101.

[2] M.-J. Sher, E.G. Hemme, Hyperdoped silicon materials: from basic materials properties to sub-bandgap infrared photodetectors, Semicond. Sci. Technol. 38 (2023) 33001, https://doi.org/10.1088/1361-6641/acb16b.

[3] P. Saring, A. Lena Baumann, B. Schlieper-Ludewig, S. Kontermann, W. Schade, M. Seibt, Electronic and structural properties of femtosecond laser sulfur hyperdoped silicon pn-junctions, Appl. Phys. Lett. 103 (2013) 61904, https://doi.org/10.1063/1.4817726.

[4] Z. Zhao, Z. Zhang, J. Jing, R. Gao, Z. Liao, W. Zhang, G. Liu, Y. Wang, K. Wang, C. Xue, Black silicon for near-infrared and ultraviolet photodetection: a review, Apl. Mater. 11 (2023) 21107, https://doi.org/10.1063/5.0133770.

[5] J.-H. Zhao, X.-B. Li, Q.-D. Chen, Z.-G. Chen, H.-B. Sun, Ultrafast laser-induced black silicon, from micro-nanostructuring, infrared absorption mechanism, to high performance detecting devices, Materials Today Nano 11 (2020) 1–20, https://doi.org/10.1016/j.mtnano.2020.100078.

[6] B. Franta, E. Mazur, S.K. Sundaram, Ultrafast laser processing of silicon for photovoltaics, Int. Mater. Rev. 63 (2018) 227–240, https://doi.org/10.1080/09506608.2017.1389547.

[7] S. Kontermann, T. Gimpel, A.L. Baumann, K.-M. Guenther, W. Schade, Laser processed black silicon for photovoltaic applications, Energy Proc. 27 (2012) 390–395, https://doi.org/10.1016/j.egypro.2012.07.082.

[8] W. Yang, J. Mathews, J.S. Williams, Hyperdoping of Si by ion implantation and pulsed laser melting, Mater. Sci. Semicond. Process. 62 (2017) 103–114, https://doi.org/10.1016/j.mssp.2016.11.005.

[9] M. Wang, Y. Berencén, E. García-Hemme, S. Prucnal, R. Hübner, Y. Yuan, C. Xu, L. Rebohle, R. Böttger, R. Heller, H. Schneider, W. Skorupa, M. Helm, S. Zhou, Extended infrared photoresponse in Te -hyperdoped Si at room temperature, Phys. Rev. Appl. 10 (2018), https://doi.org/10.1103/PhysRevApplied.10.024054.

[10] C.-H. Li, J.-H. Zhao, Q.-D. Chen, J. Feng, W.-T. Zheng, H.-B. Sun, Infrared absorption of femtosecond laser textured silicon under vacuum, IEEE Photon. Technol. Lett. 27 (2015) 1481–1484, https://doi.org/10.1109/LPT.2015.2425953.

[11] I. Umezu, J.M. Warrender, S. Charnvanichborikarn, A. Kohno, J.S. Williams, M. Tabbal, D.G. Papazoglou, X.-C. Zhang, M.J. Aziz, Emergence of very broad infrared absorption band by hyperdoping of silicon with chalcogens, J. Appl. Phys. 113 (2013) 213501, https://doi.org/10.1063/1.4804935.

[12] C.B. Simmons, A.J. Akey, J.J. Krich, J.T. Sullivan, D. Recht, M.J. Aziz, T. Buonassisi, Deactivation of metastable single-crystal silicon hyperdoped with sulfur, J. Appl. Phys. 114 (2013) 1–8, https://doi.org/10.1063/1.4854835.

[13] C. Li, J.-H. Zhao, Z.-G. Chen, Infrared absorption and sub-bandgap photo-response of hyperdoped silicon by ion implantation and ultrafast laser melting, J. Alloys Compd. 883 (2021) 160765, https://doi.org/10.1016/j.jallcom.2021.160765.

[14] A. Debernardi, Engineering the insulator-to-metal transition by tuning the population of dopant defects: first principles simulations of Se hyperdoped Si, Semicond. Sci. Technol. 38 (2023) 14002, https://doi.org/10.1088/1361-6641/ac9db7.

[15] G. Haberfehlner, M.J. Smith, J.-C. Idrobo, G. Auvert, M.-J. Sher, M.T. Winkler, E. Mazur, N. Gambacorti, S. Gradečak, P. Bleuet, Selenium segregation in femtosecond-laser hyperdoped silicon revealed by electron tomography, Microsc. Microanal. 19 (2013) 716–725, https://doi.org/10.1017/S1431927613000342.

[16] Z. Hu, J. Fu, L. Cheng, D. Ding, J. Cong, D. Yang, X. Yu, The mechanism behind the annealing-induced reduction of infrared absorption in zinc-hyperdoped silicon, phys. stat. sol. a (2024) 2300738, https://doi.org/10.1002/pssa.202300738.

[17] S. Zhou, F. Liu, S. Prucnal, K. Gao, M. Khalid, C. Baehtz, M. Posselt, W. Skorupa, M. Helm, Hyperdoping silicon with selenium: solid vs. liquid phase epitaxy, Sci. Rep. 5 (2015) 8329, https://doi.org/10.1038/srep08329.

[18] J.E. Carey, C.H. Crouch, M. Shen, E. Mazur, Visible and near-infrared responsivity of femtosecond-laser microstructured silicon photodiodes, Opt. Lett. 30 (2005) 1773–1775, https://doi.org/10.1364/OL.30.001773.

[19] Z. Huang, J.E. Carey, M. Liu, X. Guo, E. Mazur, J.C. Campbell, Microstructured silicon photodetector, Appl. Phys. Lett. 89 (2006) 33506, https://doi.org/10.1063/1.2227629.

[20] S. Huang, Q. Wu, Z. Jia, X. Jin, X. Fu, H. Huang, X. Zhang, J. Yao, J. Xu, Black silicon photodetector with excellent comprehensive properties by rapid thermal annealing and hydrogenated surface passivation, Adv. Opt. Mater. (2020) 1–7, https://doi.org/10.1002/adom.201901808.

[21] K.-F. Wang, P. Liu, S. Qu, Y. Wang, Z. Wang, Optical and electrical properties of textured sulfur-hyperdoped silicon: a thermal annealing study, J. Mater. Sci. 50 (2015) 3391–3398, https://doi.org/10.1007/s10853-015-8895-2.

[22] S. Paulus, P. Mc Kearney, F. Völklein, S. Kontermann, Obtaining simultaneously high crystallinity and sub-bandgap absorption in femtosecond laser hyperdoped black silicon using ion beam etching, AIP Adv. 11 (2021) 75014, https://doi.org/10.1063/5.0044678.

[23] E. Janzén, R. Stedman, G. Grossmann, H.G. Grimmeiss, High-resolution studies of sulfur- and selenium-related donor centers in silicon, Phys. Rev. B 29 (1984) 1907–1918, https://doi.org/10.1103/PhysRevB.29.1907.

[24] M.V. Limaye, S.C. Chen, C.Y. Lee, L.Y. Chen, S.B. Singh, Y.C. Shao, Y.F. Wang, S.H. Hsieh, H.C. Hsueh, J.W. Chiou, C.H. Chen, L.Y. Jang, C.L. Cheng, W.F. Pong, Y.F. Hu, Understanding of sub-band gap absorption of femtosecond-laser sulfur hyperdoped silicon using synchrotron-based techniques, Sci. Rep. (2015) 1–12, https://doi.org/10.1038/srep11466.

[25] B.K. Newman, M.-J. Sher, E. Mazur, T. Buonassisi, Reactivation of sub-bandgap absorption in chalcogen-hyperdoped silicon, Appl. Phys. Lett. (2011) 1–3, https://doi.org/10.1063/1.3599450.

[26] B.Y. Cao, H.W. Yang, Y.J. Chen, Y.B. Lin, Y.J. Yang, C. Wen, W.B. Yang, Thermal activation mechanism of sulfur impurities in sulfur-hyperdoped silicon films, Mater. Sci. Semicond. Process. (2022) 1–8, https://doi.org/10.1016/j.mssp.2022.107112.

[27] B. Franta, D. Pastor, H.H. Gandhi, P.H. Rekemeyer, S. Gradečak, M.J. Aziz, E. Mazur, Simultaneous high crystallinity and sub-bandgap optical absorptance in hyperdoped black silicon using nanosecond laser annealing, J. Appl. Phys. 118 (2015) 1–10, https://doi.org/10.1063/1.4937149.

[28] S. Paulus, M. Roser, P. McKearney, M. Will, S. Schäfer, S. Kontermann, Classification of different post-hyperdoping treatments for enhanced crystallinity of IR-sensitive femtosecond-laser processed silicon, Semicond. Sci. Technol. 38 (2023) 24002, https://doi.org/10.1088/1361-6641/acad93.

[29] P. Mc Kearney, S. Schäfer, S. Paulus, M. Roser, F. Piermaier, I. Lebershausen, S. R. Kontermann, Ultrafast laser heating for controlling the optoelectronic properties of sulfur hyperdoped black silicon, J. Appl. Phys. 133 (2023) 13102, https://doi.org/10.1063/5.0130743.

[30] Simon Paulus, Patrick McKearney, Sören Schäfer, Tobias Niemeyer, Michael Roser, Fabian Piermaier, Ingo Lebershausen, Michael Seibt, Stefan Kontermann, Evolution of Carrier Mobility and Density in Laser Sulfur Hyperdoped Silicon after Different Post-laser Treatments, Strasbourg, 2023.

[31] S.Q. Lim, J.S. Williams, Electrical and optical doping of silicon by pulsed-laser melting, Micro 2 (2022) 1–22, https://doi.org/10.3390/micro2010001.

[32] M. Wang, R. Hübner, C. Xu, Y. Xie, Y. Berencén, R. Heller, L. Rebohle, M. Helm, S. Prucnal, S. Zhou, Thermal stability of Te-hyperdoped Si: atomic-scale correlation of the structural, electrical, and optical properties, Phys. Rev. Mater. 3 (2019), https://doi.org/10.1103/PhysRevMaterials.3.044606.

[33] C. Wen, W. Chen, Y.P. Chen, K.J. Liu, X.H. Li, S.F. Hu, Y.J. Yang, Thermal annealing performance of sulfur-hyperdoped black silicon fabricated using a Nd: YAG nanosecond-pulsed laser, Mater. Res. Bull. 93 (2017) 238–244, https://doi.org/10.1016/j.materresbull.2017.05.011.

[34] S. Schäfer, P. McKearney, S. Paulus, S. Kontermann, Analytical model for extracting optical properties from absorptance of femtosecond-laser structured hyperdoped silicon, J. Appl. Phys. 131 (2022) 243102, https://doi.org/10.1063/5.0094177.

[35] K.-M. Guenther, T. Gimpel, S. Kontermann, W. Schade, Investigation of the sulfur doping profile in femtosecond-laser processed silicon, Appl. Phys. Lett. 102 (2013) 1–4, https://doi.org/10.1063/1.4807679.

[36] R.O. Carlson, R.N. Hall, E.M. Pell, Sulfur in silicon, J. Phys. Chem. Solid. 8 (1959) 81–83, https://doi.org/10.1016/0022-3697(59)90279-3.

[37] B.R. Tull, M.T. Winkler, E. Mazur, The role of diffusion in broadband infrared absorption in chalcogen-doped silicon, Appl. Phys. A 96 (2009) 327–334, https://doi.org/10.1007/s00339-009-5200-8.

[38] J.F. Morhange, G. Kanellis, M. Balkanski, J.F. Peray, J. Icole, M. Croset, Raman Spectroscopy of Pulsed-laser annealed ion implanted silicon, in: AIP Conference Proceedings, AIP, 1979, pp. 429–433.

[39] D.M. Caughey, R.E. Thomas, Carrier mobilities in silicon empirically related to doping and field, Proc. IEEE 55 (1967) 2192–2193, https://doi.org/10.1109/PROC.1967.6123.

[40] D. Stieler, V.L. Dalal, K. Muthukrishnan, M. Noack, E. Schares, Electron mobility in nanocrystalline silicon devices, J. Appl. Phys. 100 (2006) 036106, https://doi.org/10.1063/1.2234545.

[41] S. Kudryashov, K. Boldyrev, A. Nastulyavichus, D. Prikhod'ko, S. Tarelkin, D. Kirilenko, P. Brunkov, A. Shakhmin, K. Khamidullin, G. Krasin, M. Kovalev, Near-far IR photoconductivity damping in hyperdoped Si at low temperatures, Opt. Mater. Express 11 (2021) 3792, https://doi.org/10.1364/OME.438023.